Journal of Industrial and Engineering Chemistry 60 (2018) 85–90

Contents lists available at ScienceDirect

Journal of Industrial and Engineering Chemistry

journal homepage: www.elsevier.com/locate/jiec

Short communication

Standalone macroporous graphitic nanowebs for vanadium redox flow batteries

Min Eui Lee[a], Sungho Lee[b], Hyoung-Joon Jin[a,*], Young Soo Yun[c,*]

[a] Department of Polymer Science and Engineering, Inha University, Incheon 22212, South Korea
[b] Carbon Composite Materials Research Center, Korea Institute of Science and Technology, Wanju-gun 55324, South Korea
[c] Department of Chemical Engineering, Kangwon National University, Samcheok 25913, South Korea

ARTICLE INFO

Article history:
Received 25 July 2017
Received in revised form 15 September 2017
Accepted 24 September 2017
Available online 3 October 2017

Keywords:
Macroporous carbon
Nanoweb
Nanoribbon
Electrode
Redox flow batteries

ABSTRACT

Vanadium redox flow batteries (VRFBs) have attracted much attention as next-generation large-scale energy storage devices. However, they suffer from a drop in the energy efficiency induced by the large activation polarization during vanadium redox reactions. In this study, we designed electrode materials with a high energy efficiency that are a macroporous monolith composed of three-dimensionally entangled graphitic nanoribbons. These materials were denoted as macroporous graphitic nanowebs (M-GNWs), possessing a high specific surface area of 213 $m^2 g^{-1}$ and a large pore volume of 0.82 $cm^3 g^{-1}$. A large number of oxygen functional groups (C/O ratio of 4.4) were introduced after immersing the M-GNWs in the acidic electrolyte used in VRFBs. These properties of M-GNWs led to beneficial electrochemical catalytic effects such as low anodic and cathodic peak potential separation ($\triangle E_p$) values of ~73.4 mV (catholyte) in a cyclic voltammetry test conducted at a sweep rate of 2 mV s^{-1}. Furthermore, the VRFBs based on an M-GNW anode and cathode pair exhibited a significantly improved energy efficiency of 85.8%, which is 12.4% higher than that (73.4%) of the commercial carbon felt-based VRFBs.

Introduction

Large-scale electric energy storage (EES) devices are becoming increasingly important for a stable and on-demand supply of clean energies generated from renewable energy resources such as solar, wind, and tidal power [1,2]. Redox flow batteries, one of the large-scale EES devices, have advantages of design flexibility for a target application and a long-term electrochemical stability owing to their unique structural feature. Their active redox-couples with a no host structure are dissolved in two separate electrolytes that are individually stored in containers of the desired sizes [3,4]. In particular, all the vanadium redox flow batteries (VRFBs) based on V^{2+}/V^{3+} and VO^{2+}/VO_2^+ redox couples for the anolyte and catholyte, respectively, show a relatively high working voltage (~1.26 V) and a low ion crossover that effectively suppresses the energy loss by self-discharge, making the VRFBs promising candidates as a large-scale EES device [5–7]. However, the VRFBs suffer from a decline in the energy efficiency originating from the large activation polarization during vanadium redox reactions, hindering their extensive application [8–10]. To address this issue, various electrode materials exhibiting catalytic effects for the vanadium redox reactions have been explored [8–20]. Among several materials, nanocarbon-based electrodes such as graphene, carbon nanotube, and electrospun carbon nanofiber showed superior catalytic effects for the vanadium redox reactions owing to their high active surface area with numerous redox-active heteroatoms and a good electrical conductivity [19–26]. The catalytic effects of the oxygen functional groups on the poly-hexagonal carbon structures are well-known and are represented in the following equations for catholyte Eq. (1) and anolyte Eq. (2) [27,28]:

$$R-OH(R-COOH)+VO^{2+}+H_2O \leftrightarrow R-OH(R-COOH)+VO_2^{+}+2H^{+}+e^{-} \quad (1)$$

$$R-OH(R-COOH)+V^{3+}+e^{-} \leftrightarrow R-OH(R-COOH)+V^{2+} \quad (2)$$

Park et al. reported that the oxygen functional groups of graphene nanoplatelets play a key role in the electrocatalytic activity of the vanadium redox couples [20]. Han et al. showed outstanding catalytic effects of the nanohybrids based on graphene oxide nanosheets and multi-walled carbon nanotubes that include a large number of oxygen functional groups [23]. It was also reported that the edge sites of the poly-hexagonal carbon

* Corresponding authors.
E-mail addresses: hjjin@inha.ac.kr (H.-J. Jin), ysyun@kangwon.ac.kr (Y.S. Yun).

https://doi.org/10.1016/j.jiec.2017.09.043
1226-086X/

structures show superior catalytic effects compared with their basal plane [29]. Hence, most of the studies highlight the intrinsic oxygen functional groups of active carbon materials with a large number of edge sites [8–13,20–24]. However, the nanocarbon-based active materials have a limitation that an additional conducting carbon substrate, e.g. carbon felt (CF), is essential for their practical use in a full-cell system. This is because their unstable carbon surfaces can be fully oxidized in strong electrolytes, resulting in non-conducting carbonaceous materials. Therefore, in order to design a feasible nanocarbon-based active electrode, it is important to realize a monolith with a highly ordered graphitic nanostructure and a large number of edge sites. In addition, a macroporous structure is inevitable to facilitate an efficient flow of vanadium-based electrolytes.

In this study, standalone macroporous graphitic nanowebs (M-GNWs) were prepared from a microbial-induced cellulose by heating at 2800 °C. The M-GNWs are composed of entangled graphitic nanofibers containing numerous carbon edge sites and a poor oxygen content (C/O ratio of 89.1). After immersion in an acidic electrolyte, the carbon structure of the M-GNWs was fully functionalized by the oxygen groups, showing superior catalytic effects for the vanadium ions compared with that of the conventional CFs. In contrast, a similar sample prepared by heating at a relatively low temperature of 1200 °C had an amorphous carbon structure, which was fully oxidized in the acidic condition, leading to poor electrochemical performances. This study reveals several important features of the electrode materials for VRFBs. They are as follows: (1) Not only the intrinsic oxygen groups on the electrode surface but also the functionalized oxygen groups under the acidic electrolyte can affect the catalytic effects of the carbon-based electrode for the redox reaction of vanadium ions, (2) Carbon microstructure is very important for the electrode stability when operated in the strong acid media, in particular for a nanostructured carbon material, and (3) Macroporous graphitic nanostructures with numerous carbon edge sites can deliver a much improved electrochemical performances compared with the typical CF electrodes.

Experimental

Preparation of microbial-induced cellulose cryogels

Microbial-induced cellulose pellicles were synthesized by *Acetobacter xylinum* BRC 5 in a Hestrin and Schramm (HS) medium using a reported procedure [30]. The cells were precultured in a test tube for 3 days. Then, 50 μL of the active cells was poured in an erlenmeyer flask with 100 mL of HS medium and was incubated at 30 °C for 7 days. To purify the cells and remove the residual HS medium, the prepared cellulose hydrogels were immersed in a 0.25 M aqueous sodium hydroxide solution (NaOH, 97.0%, Daejung, Republic of Korea) for 2 days at room temperature. The purified cellulose hydrogels were then neutralized by washing with deionized water and immersed in *tert*-butanol at room temperature. After freezing at −30 °C for 6 h, the frozen cellulose pellicles were freeze-dried at −45 °C and 4.5 Pa for 3 days.

Preparation of M-GNWs

The as-prepared cellulose cryogels were heated to 1200 °C in a tubular furnace for 2 h. A heating rate of 5 °C min^{-1} and an Ar flow of 200 mL min^{-1} were applied during the heating process. The resultant product was named as M-CNWs. The M-CNWs were further heated to 2800 °C in a graphite furnace under an Ar atmosphere. After loading the M-CNWs into the graphite furnace, step by step heating rates of 10, 5, and 3 °C min^{-1} were applied up to 1800, 2300, and 2800 °C, respectively. The final product (M-GNW) was stored in a vacuum oven at 30 °C without further treatment.

Characterization

Morphologies of the samples were examined by field-emission scanning electron microscopy (FE-SEM, S-4300, Hitachi, Japan) and field-emission transmission electron microscopy (FE-TEM, JEM2100F, JEOL, Japan). X-ray diffraction (XRD, DMAX-2500, Rigaku,) analysis of the samples was performed using Cu-K_α radiation (wavelength $\lambda = 0.154$ nm) at 40 kV and 100 mA. Raman spectra were recorded using a continuous-wave linearly polarized laser (514.5 nm wavelength, 2.41 eV, 16 mW power). The laser beam was focused by a 100 × objective lens, resulting in a spot of ~1 μm diameter. Acquisition time and number of circulations to collect each spectrum were 10 s and 5 cycles, respectively. The porous properties of the samples were analyzed using nitrogen adsorption and desorption isotherms that were obtained using surface area and porosimetry analyzer (ASAP 2020, Micromeritics, USA) at −196 °C. The chemical composition of the samples was examined by X-ray photoelectron spectroscopy (XPS, PHI 5700 ESCA, USA) with a monochromatic Al Kα radiation ($h\nu = 1486.6$ eV).

Electrochemical characterization

The electrochemical performance of the samples and their flow-cell devices were characterized with the aid of a potentiostat (PGSTAT302N, Autolab), Wonatech automatic battery cycler, and single-cell test equipment (Standard Cell — Blue, Standard Energy Co., Ltd., South Korea). For the half-cell, a hand-made, three-electrode configuration system was used as shown in Fig. S1 [31]. The M-CNWs and M-GNWs with a diameter of 5 mm (area: 0.196 cm^2), commercial CFs (c-CF, XF-30A, thickness: 4.3 mm, Toyobo, Japan), and Ag/AgCl were used as the working, counter, and reference electrodes, respectively. $VOSO_4$ (0.1 M, 99.5%, Sigma-Aldrich) was dissolved in H_2SO_4 (2 M, 96.5%, Sigma-Aldrich) and was used as the electrolyte for the half-cell tests. For a full-cell test, a single cell based on a symmetric M-GNW//M-GNW electrode pair was assembled with copper current collectors, bipolar plates, and cation exchange membranes (Nafion 115, DuPont Co., Ltd., USA). The working electrodes with an area of 4 cm^2 were used as both cathode and anode. The electrolyte was prepared by dissolving 1.6 M $VOSO_4$ in 4 M H_2SO_4 solution and a volume of 60 mL was taken in each of the catholyte and anolyte tanks. Optical image of a single flow cell is shown in Fig. S2. Galvanostatic charge/discharge and cyclic voltammetry tests of the single flow cell were performed at various current densities and sweep rates, respectively. Similar tests were conducted using c-CF pair as electrodes for comparison.

Results and discussion

Morphologies of M-CNWs and M-GNWs characterized by FE-SEM are shown in Fig. 1(a) and (b). Both the samples show a similar three-dimensional macroporous structure composed of entangled nanofibers with diameters of about 10–20 nm. It is noteworthy that despite a high temperature heating at ~2800 °C, the initial macroporous structure of M-GNWs is well-maintained. On the contrary to the pore structure, the microstructure of M-GNWs is distinguished from that of M-CNWs. The FE-TEM image of M-CNWs reveals an amorphous carbon structure without a long-range carbon ordering [Fig. 1(c)], while M-GNWs exhibit an ordered graphitic nanoribbon structure [Fig. 1(d)]. Further, the specific differences in microstructures were investigated by Raman spectra and XRD patterns [Fig. 2(a) and (b)]. The Raman spectra of M-CNWs and M-GNWs show distinct *D* and *G* bands. The *D* bands represent the intrinsic phonon modes with the A_{1g} symmetry of

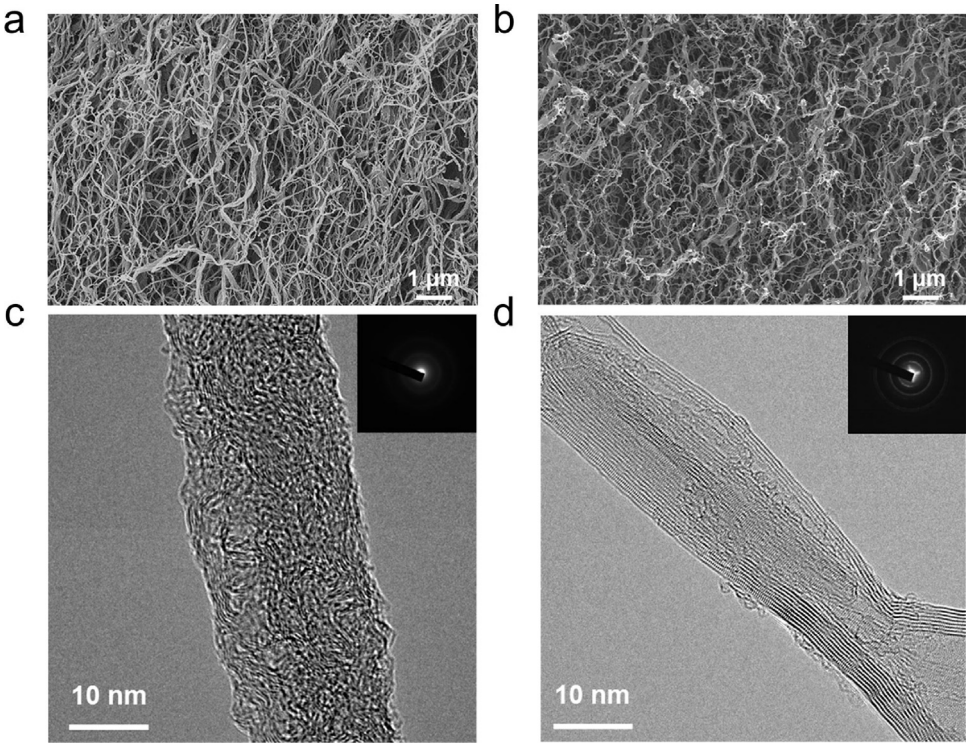

Fig. 1. Morphological characteristics of the M-CNWs and M-GNWs. (a), (b) FE-SEM and (c), (d) FE-TEM images of M-CNWs and M-GNWs.

the infinite aromatic ring that is activated by the structural disorder and *G* bands represent the hexagonal structure related to the E_{2g} vibration mode of the sp^2-hybridized C atoms [Fig. 2(a)] [32]. The *D* and *G* bands of M-CNWs are broad and connected with each other, while that of M-GNWs are relatively sharp and separate. In addition, the *D* to *G* intensity ratio (I_D/I_G) of M-CNWs is 1.02 which is much larger than that of M-GNWs (0.28). These results indicate that M-GNWs have a much more ordered hexagonal carbon structure than M-CNWs. The approximate size of the ordered hexagonal carbon layers for M-CNWs and M-GNWs as calculated from the Raman bands corresponds to about 4.4 and 15.7 nm [33,34]. In addition, the XRD pattern of M-GNWs shows a relatively sharp graphite (002) peak at 25.7°, which is in contrast with the broad pattern of M-CNWs [Fig. 2(b)]. These results

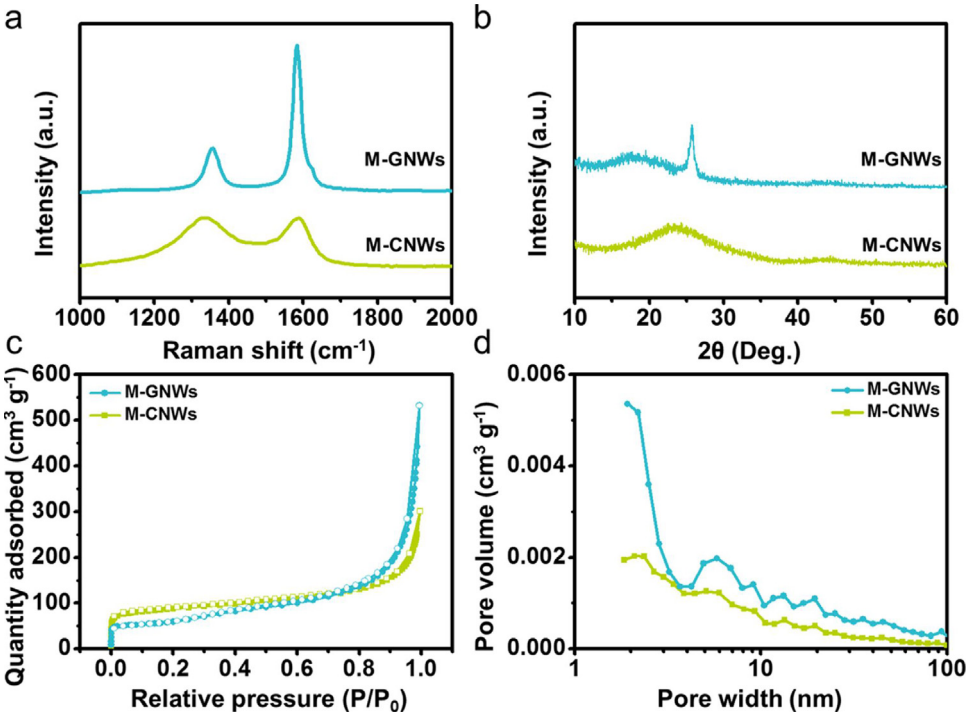

Fig. 2. (a) Raman spectra and (b) XRD pattern of M-CNWs and M-GNWs. (c) Nitrogen adsorption and desorption isotherms of M-CNWs and M-GNWs, and (d) pore size distribution data of M-CNWs and M-GNWs.

indicate that M-GNWs have a more ordered graphitic structure than M-CNWs.

The pore structure of M-CNWs and M-GNWs was characterized using nitrogen adsorption and desorption isotherm curves [Fig. 2(c)]. In a low relative pressure region of <0.02, a sharp increase in the adsorbed nitrogen quantity of ~70 and ~45 $cm^3 g^{-1}$ was observed for M-CNWs and M-GNWs, respectively. This adsorption of nitrogen molecules at a low relative pressure is attributed to their monolayer adsorption on the surface of M-CNWs and M-GNWs [35]. Owing to a more disordered carbon structure with smaller hexagonal carbon domains, M-CNWs can have a larger monolayer adsorption quantity than that of M-GNWs. In addition, both the isotherms show a dramatic increase in the adsorbed nitrogen quantity in a high relative pressure region above 0.9 and a small hysteresis between the adsorption and desorption curves. These results indicate that both M-CNWs and M-GNWs are mainly macroporous structures corresponding to IUPAC type-II [36]. The pore size distribution data of M-CNWs and M-GNWs exhibit that they have numerous pores with various pore widths [Fig. 2(d)]. The specific surface area of M-CNWs and M-GNWs is 317 and 213 $m^2 g^{-1}$, respectively, which are about 160 and 110 times higher than that of c-CFs. Furthermore, the pore volume of M-GNWs is ~0.82 $cm^3 g^{-1}$, which is about 1.8 and 82 times higher than that of M-CNWs and c-CFs, respectively. The detailed textural properties of M-CNWs and M-GNWs are recorded in Table S1.

The surface properties of M-CNWs and M-GNWs were investigated by XPS [Fig. 3]. The XPS C 1s spectra of M-CNWs and M-GNWs show several similar configurations such as C=C, C—C, C—O, and O—C=O bonding [Fig. 3(a) and (b)], while C/O ratios in both the samples are significantly different, i.e., 11.2 and 89.9 for M-CNWs and M-GNWs, respectively [Fig. 3(c)]. It is also noteworthy that the surface properties of M-CNWs and M-GNWs were highly affected by immersing them into the acidic electrolyte. After soaking both the samples in the electrolyte containing 2 M H_2SO_4 for 12 h, their surface carbon strongly oxidized, thereby, the C/O ratios of M-CNWs and M-GNWs dramatically decreased to 1.3 and 4.4, respectively [Fig. 3(c)]. The detailed surface properties are shown in Table S2. Additionally, the XPS O 1s spectra of M-CNWs and M-GNWs are added in Fig. S3, which shows that the oxygen configurations in both the samples are similar to each other. The changed surface properties after immersion in the electrolyte strongly affected their electrochemical performances.

The electrochemical performances of M-CNWs and M-GNWs were measured by using a hand-made three-electrode configuration system using a 0.1 M $VOSO_4$ dissolved in 2 M H_2SO_4 solution as the electrolyte over the voltage windows between 0.4 and 1.3 V vs. Ag/AgCl [Fig. 4]. The cyclic voltammetry (CV) curves of c-CFs and M-GNWs conducted at a sweep rate of 2 mV s^{-1} show distinct anodic and cathodic peaks. The peak potential separation ($\triangle E_p$) is ~130 mV and ~73.4 mV in catholyte for c-CFs and M-GNWs, respectively [Fig. 4(a)]. A better catalytic effect of M-GNWs could be induced from the unique nanostructure with numerous edge sites that are functionalized by the oxygen groups in the acidic electrolyte. As shown in Fig. 4(b), the slopes of the sweep rate versus the oxidation and reduction peak current density plots also are larger for M-GNWs than for c-CFs in catholyte, indicating better performances in M-GNWs. In contrast, M-CNWs are fully oxidized in the acidic condition, thus exhibiting poor electrochemical performances owing to the deteriorated electrical properties [Fig. S4]. The practicability of M-GNWs as electrodes for VRFBs was further tested in full-cell VRFB systems that were assembled using the same M-GNW electrode pairs for both anolyte and

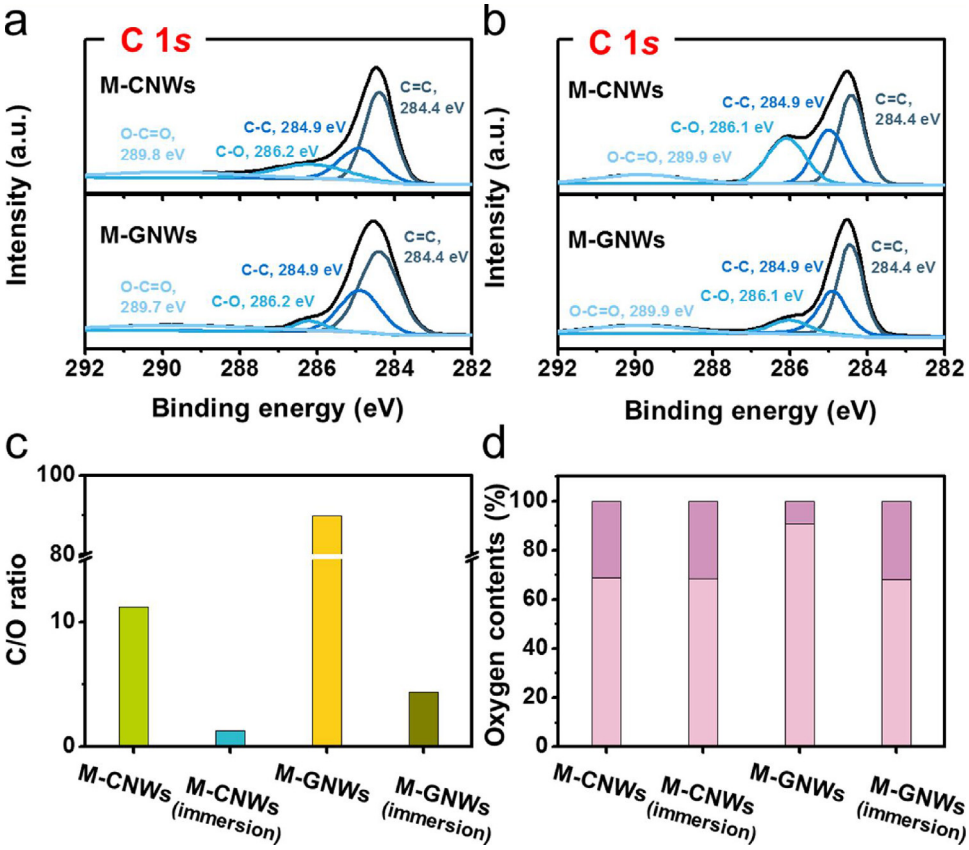

Fig. 3. XPS analysis of the M-CNWs and M-GNWs. High-resolution spectra of (a) C 1s (as-prepared) and (b) C 1s (after immersion in electrolyte). (c) Chemical composition ratio of heteroatoms and (d) chemical composition contents of functional groups from O 1s spectra for M-CNWs and M-GNWs.

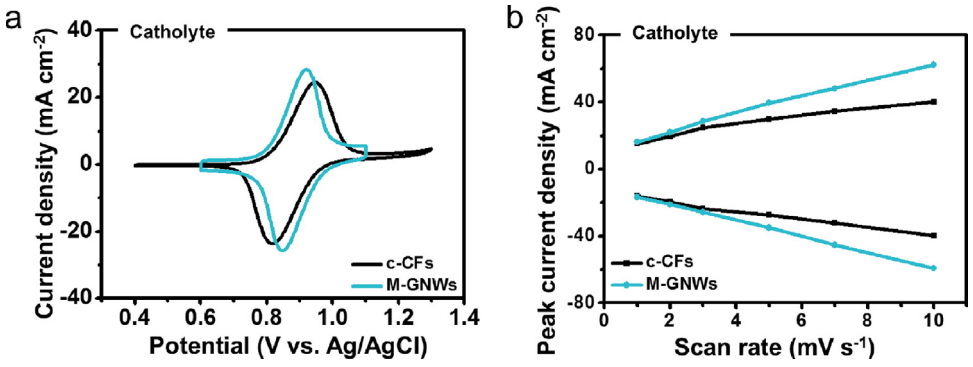

Fig. 4. Cyclic voltammetry with c-CF and M-GNW electrodes for (a) VO^{2+}/VO_2^+ redox couple in 0.1 M $VOSO_4$ + 2 M H_2SO_4 aqueous solution at a sweep rate of 2 mV s^{-1}, respectively. (b) Peak current densities of c-CFs and M-GNWs in catholyte.

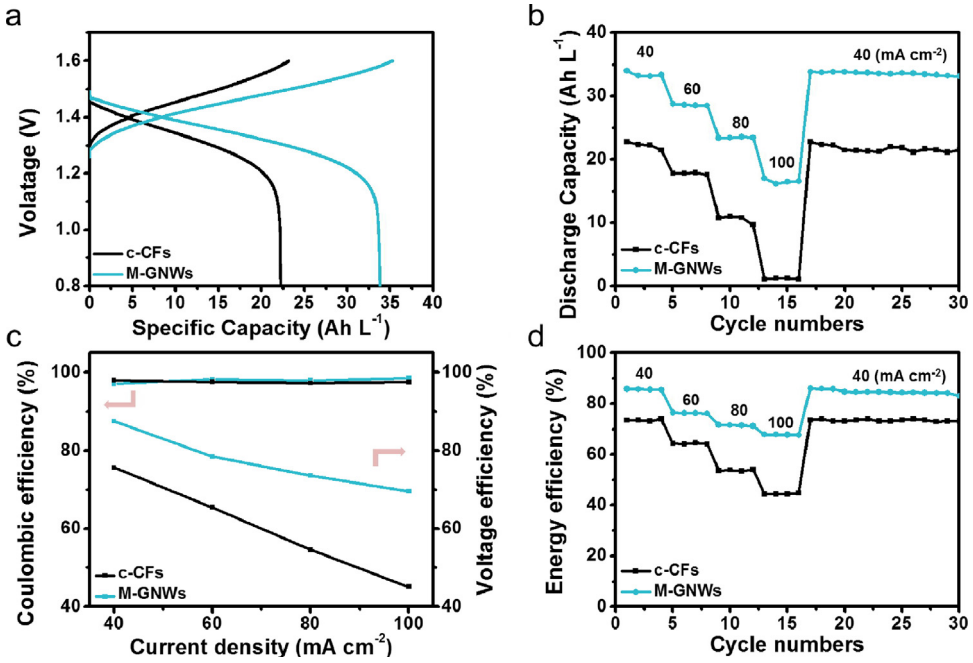

Fig. 5. Electrochemical performance of VRFB employing the c-CF and M-GNW electrodes in flow-type single cell at room temperature: (a) Charge-discharge profiles at current density of 40 mA cm^{-2}. (b) Discharge capacity of VRFBs with each electrode as functions of cycle number at different current densities. (c) Coulombic and voltage efficiency at current densities in the range of 40–100 mA cm^{-2}. (d) Energy efficiencies (EE) of c-CF and M-GNW electrodes in a VRFB single cell operation for a continuous charge-discharge cycles at different current densities.

catholyte [Fig. S5]. The electrochemical performance of this assembly was compared with that of the c-CF electrode pair system. The galvanostatic charge/discharge profiles of c-CFs- and M-GNWs-based VRFBs characterized in a voltage window between 0.8 and 1.6 V are exhibited in Fig. 5(a). The profiles show a considerable gap in their specific capacities. M-GNWs-based VRFBs exhibit a specific capacity of 34.2 Ah L^{-1} at 40 mA cm^{-2} corresponding to ~150% of that (22.7 Ah L^{-1}) of c-CFs-based VRFBs [Fig. 5(a)]. Note that M-GNWs-based VRFBs have superior rate capabilities at current densities from 40 to 100 mA cm^{-2}, as shown in Fig. 5(b). While c-CFs showed an abrupt decrease at the current density of 100 mA cm^{-2}, M-GNWs-based VRFBs maintained ~50% of their initial capacity. In addition, when the current density is returned to 40 mA cm^{-2} after 16 cycles with a continuous increase in the current rates, the initial specific capacity value of M-GNWs-based VRFBs was fully recovered, indicating the high reversibility of the capacity. Moreover, M-GNWs-based VRFBs revealed a high voltage efficiency of ~87.5%, which is about ~11.9% higher than that of c-CFs-based VRFBs (75.6%) [Fig. 5(c)]. Because both the systems have a high Coulombic efficiency of above 98%, their energy efficiency is highly dependent on the voltage efficiency. Thereby, M-GNWs-based VRFBs showed higher energy efficiencies at all the current densities from 40 to 100 mA cm^{-2}, as shown in Fig. 5(d). A maximum energy efficiency of 85.8% and 73.4% was achieved for M-GNWs- and c-CFs-based VRFBs, respectively. In addition, stable cycles were maintained over 30 cycles. These results demonstrate that M-GNWs have a great potential as an electrode for VRFBs.

Conclusion

In summary, monolithic M-GNWs were fabricated from freeze-dried microbial cellulose pellicles by heating at 2800 °C. M-GNWs have a three-dimensional macroporous structure composed of entangled graphitic nanofibers with diameters of about 10–20 nm and numerous carbon edge sites. In addition, M-GNWs have a high specific surface area of 213 $m^2 g^{-1}$ and a large pore volume of 0.82 $cm^3 g^{-1}$, which are ~110 and 82 times higher than those of c-

CFs, respectively. After the M-GNWs were immersed in the acidic electrolyte, numerous oxygen functional groups were introduced to their surface carbon structures, leading to high catalytic effects with a $\triangle E_p$ value of ~73.4 mV (catholyte) in a CV test conducted at 2 mV s^{-1}. In addition, M-GNW-based VRFBs demonstrated their feasible electrochemical performances such as high voltage, Coulombic, and energy efficiencies of 87.5, 98.0, and 85.8%, respectively, which was superior to those of the c-CFs-based VRFBs.

Acknowledgments

This research was supported by Basic Science Research Program through the National Research Foundation of Korea (NRF) funded by the Ministry of Education (NRF-2016R1A2B4009601) and (NRF-2017R1C1B1004167), and the Korea Institute of Energy Technology Evaluation and Planning (KETEP) and the Ministry of Trade, Industry & Energy (MOTIE) of the Republic of Korea (No. 20145020300980).

Appendix A. Supplementary data

Supplementary data associated with this article can be found, in the online version, at https://doi.org/10.1016/j.jiec.2017.09.043.

References

[1] B. Dunn, H. Kamath, J.-M. Tarascon, Science 334 (2012) 928.
[2] D. Larcher, J.-M. Tarascon, Nat. Chem. 7 (2015) 19.
[3] K. Lin, Q. Chen, M.R. Gerhardt, L. Tong, S.B. Kim, L. Eisenach, A.W. Valle, D. Hardee, R.G. Gordon, M.J. Aziz, M.P. Marshak, Science 349 (2015) 1529.
[4] M. Park, J. Ryu, W. Wang, J. Cho, Nat. Rev. Mater. 2 (2016) 16080.
[5] M. Skyllas-Kazacos, M. Rychcik, R.G. Robins, A.G. Fane, J. Electrochem. Soc. 133 (1986) 1057.
[6] M. Skyllas-Kazacos, M. Grossmith, J. Electrochem. Soc. 134 (1987) 2950.
[7] L. Li, S. Kim, W. Wang, M. Vijayakumar, Z. Nie, B. Chen, J. Zhang, G. Xia, J. Hu, G. Graff, J. Liu, Z. Yang, Adv. Energy Mater. 1 (2011) 394.
[8] J.J. Park, J.H. Park, O.O. Park, J.H. Yang, Carbon 110 (2016) 17.
[9] K.J. Kim, H.S. Lee, J. Kim, M.-S. Park, J.H. Kim, Y.-J. Kim, M. Skyllas-Kazacos, ChemSusChem 9 (2016) 1329.
[10] L. Estevez, D. Reed, Z. Nie, A.M. Schwarz, M.I. Nandasiri, J.P. Kizewski, W. Wang, E. Thomsen, J. Liu, J.-G. Zhang, V. Sprenkle, B. Li, ChemSusChem 9 (2016) 1455.
[11] J. Kim, H. Lim, J.-Y. Jyoung, E.-S. Lee, J.S. Yi, D. Lee, Carbon 111 (2017) 592.
[12] D. Dixon, D.J. Babu, J. Langner, M. Bruns, L. Pfaffmann, A. Bhaskar, J.J. Schneider, F. Scheiba, H. Ehrenberg, J. Power Sources 332 (2016) 240.
[13] K.J. Kim, S.-W. Lee, T. Yim, J.-G. Kim, J.W. Choi, J.H. Kim, M.-S. Park, Y.-J. Kim, Sci. Rep. 4 (2014) 6906.
[14] B. Li, M. Gu, Z. Nie, X. Wei, C. Wang, V. Sprenkle, W. Wang, Nano Lett. 14 (2014) 158.
[15] D.M. Kabtamu, J.-Y. Chen, Y.-C. Chang, C.-H. Wang, J. Mater. Chem. A 4 (2016) 11472.
[16] M. Park, J. Ryu, Y. Kim, J. Cho, Energy Environ. Sci. 7 (2014) 3727.
[17] L. Wu, Y. Shen, L. Yu, J. Xi, X. Qiu, Nano Energy 28 (2016) 19.
[18] S. Park, H. Kim, J. Mater. Chem. A 3 (2015) 12276.
[19] M. Park, I.-Y. Jeon, J. Ryu, H. Jang, J.-B. Back, J. Cho, Nano Energy 26 (2016) 233.
[20] M. Park, I.-Y. Jeon, J. Ryu, J.-B. Back, J. Cho, Adv. Energy Mater. 5 (2015) 1401550.
[21] Z. González, C. Flox, C. Blanco, M. Granda, J.R. Morante, R. Menéndez, R. Santamaría, J. Power Sources 338 (2017) 155.
[22] W. Li, Z. Zhang, Y. Tang, H. Bian, T.-W. Ng, W. Zhang, C.-S. Lee, Adv. Sci. 3 (2016) 1500276.
[23] P. Han, Y. Yue, Z. Liu, W. Xu, L. Zhang, H. Xu, S. Dong, G. Cui, Energy Environ. Sci. 4 (2011) 4710.
[24] M. Park, Y.-J. Jung, J. Kim, H.I. Lee, J. Cho, Nano Lett. 13 (2013) 4833.
[25] I. Mustafa, I. Lopez, H. Younes, R.A. Susantyoko, R.A. Al-Rub, S. Almheiri, Electrochim. Acta 230 (2017) 222.
[26] G. Wei, X. Fan, J. Liu, C. Yan, J. Power Sources 270 (2014) 634.
[27] L. Yue, W. Li, F. Sun, L. Zhao, L. Xing, Carbon 48 (2010) 3079.
[28] W. Zhang, J. Xi, Z. Li, H. Zhou, L. Liu, Z. Wu, X. Qiu, Electrochim. Acta 89 (2013) 429.
[29] N. Pour, D.G. Kwabi, T. Carney, R.M. Darling, M.L. Perry, Y. Shao-Horn, J. Phys. Chem. C 119 (2015) 5311.
[30] Y.S. Yun, H. Bak, H.-J. Jin, Synth. Met. 160 (2010) 561.
[31] J.H. Park, J.J. Park, O.O. Park, C.-S. Jin, J.H. Yang, J. Power Sources 310 (2016) 137.
[32] Y.S. Yun, G. Yoon, M. Park, S.Y. Cho, H.-D. Lim, H. Kim, Y.W. Park, B.H. Kim, K. Kang, H.-J. Jin, NPG Asia Mater. 8 (2016) e338.
[33] G.A. Zickler, B. Smarsly, N. Gierlinger, H. Peterlik, O. Paris, Carbon 44 (2006) 3239.
[34] L.G. Cançado, K. Takai, T. Enoki, Appl. Phys. Lett. 88 (2006) 163106.
[35] H.J. Yoon, M.E. Lee, N.R. Kim, S.J. Yang, H.-J. Jin, Y.S. Yun, Electrochim. Acta 242 (2017) 38.
[36] M.Y. Song, N.R. Kim, S.Y. Cho, H.-J. Jin, Y.S. Yun, ACS Sustain. Chem. Eng. 5 (2017) 616.